Dalton Transactions

ROYAL SOCIETY OF CHEMISTRY

PAPER

View Article Online
View Journal | View Issue

Check for updates

Cite this: *Dalton Trans.*, 2025, **54**, 2471

Study of methylene blue removal and photocatalytic degradation on zirconia thin films modified with Mn-Anderson polyoxometalates

Jiress Florez,[a] Carlos Diaz-Uribe,[a] William Vallejo, *[a] Freider Duran,[a] Esneyder Puello,[b] Javier Salazar,[c] Ximena Zarate[d] and Eduardo Schott *[c]

Received 2nd October 2024,
Accepted 27th November 2024

DOI: 10.1039/d4dt02782e

rsc.li/dalton

Recalcitrant pollutants are challenging to degrade during water treatment processes. Methylene blue (MB), a cationic dye, is particularly resistant to degradation and is environmentally persistent. Heterogeneous photocatalysis has emerged as a suitable strategy for removing such pollutants from water. In this work, ZrO_2 thin films were modified with Anderson-type Mn-polyoxometalate (MnPOM) ($(NH_4)_3[MnMo_6O_{24}H_6]$), and the efficiency of MB removal from water was studied. ZrO_2 was synthesized by a sol–gel method, with thin films deposited using the doctor blade method, and ZrO_2 thin films were modified using chemisorption method. The synthesized materials were characterized using SEM, EDX, UV-Vis diffuse reflectance spectroscopy and FTIR. The adsorption kinetics and isotherms for MB were studied for both bare ZrO_2 and ZrO_2/MnPOM composites. Optical characterization showed a band gap energy of 4.02 eV for bare ZrO_2, while the ZrO_2/MnPOM composite exhibited a band gap of 3.7 eV. Furthermore, ZrO_2 showed lower MB removal capacity (~8%) than ZrO_2/MnPOM thin films (~29%). The isothermal adsorption studies indicated that MB adsorption onto both bare ZrO_2 and ZrO_2/MnPOM followed the Langmuir adsorption model (q_m = 20.6 mg g^{-1} for ZrO_2 and q_m = 62.9 mg g^{-1} for ZrO_2/MnPOM). Furthermore, the adsorption kinetics of MB were well described by a pseudo-second-order model. Photocatalytic testing under UV irradiation showed an apparent rate constant (k_{ap}) of 2 × 10^{-3} min^{-1} for bare ZrO_2 and a value of k_{ap} 5.4 × 10^{-3} min^{-1} for ZrO_2/MnPOM after 100 minutes. TD-DFT calculations revealed an LMCT interaction between the ZrO_2 nanoparticle and the MnPOM, which likely contributes to the enhanced photocatalytic activity of the ZrO_2/MnPOM composite.

1. Introduction

Exponential population growth, industrialization, and unsustainable agricultural practices have intensified the global issue of water pollution, leading to significant environmental impacts on both human health and ecosystems.[1,2] Industries such as textiles, cosmetics, food processing, and pharmaceuticals are major contributors to freshwater pollution, primarily due to their high water consumption and the discharge of dyes into effluents without efficient water treatment.[3,4] Over the past decade, a special group of compounds called recalcitrant compounds have emerged as a critical target for environmental research owing to their stability and resistance to degradation by conventional treatment methods.[5,6] MB, a common cationic dye, is of particular concern due to its environmental persistence, toxicity, carcinogenicity and mutagenicity.[7] Conventional strategies for water treatment for addressing such pollutants include (i) adsorption, (ii) filtration, (iii) thermal separation, (iv) coagulation, (v) biological treatment, (vi) chemical oxidation and (vii) photochemical oxidation.[8] Advanced oxidation processes (AOPs) represent green strategies for the treatment of contaminated samples containing recalcitrant compounds due to their high oxidative capacity. These processes are non-selective and versatile and can be combined with other technologies. However, one of the drawbacks of AOPs is their substantial energy requirement, particularly for UV irradiation.[9] The physicochemical phenomenon of AOPs relies on the generation of reactive oxygen species (ROS) on the catalyst surface. These ROS are highly reactive and capable of degrading a wide range of recalcitrant

[a]*Grupo de Investigación en Fotoquímica y Fotobiología, Programa de Química, Facultad de Ciencias Básicas, Universidad del Atlántico, Puerto Colombia, 081007, Colombia. E-mail: williamvallejo@mail.uniatlantico.edu.co*
[b]*Grupo de Investigación en Oxi/Hidrotratamiento Catalítico y Nuevos Materiales, Programa de Química. Facultad de Ciencias Básicas. Universidad del Atlántico, Puerto Colombia, 081007, Colombia*
[c]*Departamento de Química Inorgánica, Facultad de Química y Farmacia, Centro de Energía UC, Centro de Investigación en Nanotecnología y Materiales Avanzados CIEN-UC, Pontificia Universidad Católica de Chile, Avenida Vicuña Mackenna, 4860 Santiago, Chile. E-mail: maschotte@gmail.com*
[d]*Instituto de Ciencias Aplicadas, Facultad de Ingeniería, Universidad Autónoma de Chile, Avenida Pedro de Valdivia 425, Santiago, Chile*

chemical compounds.[10,11] Heterogeneous catalytic processes can be considered as AOPs when a semiconductor is used as a catalyst. Specifically, the semiconductor can generate ROS upon absorbing radiation with energy exceeding its band gap value.[12,13] Among oxide semiconductors, TiO_2 and ZnO are the most studied photocatalysts in the field, due to their activity and stability.[14,15] However, other semiconductors such as zirconia (ZrO_2) have great potential to be used as photocatalysts due to their special and favorable chemical and physical properties (*e.g.*, acid–base properties and high redox properties, high density, high resistance to fracture, thermal stability, photochemical stability, and high refraction index).[16] ZrO_2 has a stable bandgap, transparency in the visible and near-infrared regions of the spectrum, and low photon energy, which reduces the probability of non-radiative decay due to multiphoton relaxation.[17] Furthermore, due to its high ion exchange capacity and redox activity, ZrO_2 exhibits a great number of oxygen vacancies on its surface.[18] However, the energy band gap of ZrO_2 is 5.0 eV, thus, this semiconductor in its pure phase is only photoactive under UV irradiation (~250 nm).[19–21] The strategies to tune the energy band gap value towards lower energy values include: (i) doping, (ii) changing the defects number, and (iii) the use of quantum dots.[22,23] The change in the number of defects can increase the specific surface area and the adsorption capacity of organic molecules.[24] After the modification of ZrO_2 with a polymorphic phase (*e.g.* monoclinic m-ZrO_2, tetragonal t-ZrO_2 and cyclic c-ZrO_2), the ions diffuse through interstitial sites inside the ZrO_2 lattice changing the conduction and valence bands values, reducing the band gap value.[25] Furthermore, reports indicate that use of the heterostructures of ZrO_2 with other materials (metals and non-metals) is another strategy to optimize its photocatalytic efficiency.[26] The doping process is another typical strategy, Chen *et al.* fabricated the Mn-doped catalyst ZrO_2/TiO_2 for the photodegradation of rhodamine B. In this report, a removal of higher than 90% after 50 minutes of UV irradiation was observed.[27] Akilandeswari *et al.* reported the synthesis of ZrO_2 doped with Mn, showing a band gap value of 2.46 eV. After the doping process, the doped ZrO_2 showed a methylene violet removal of 95% under visible irradiation. Reddy *et al.* fabricated nanoparticles of Mg-doped t-ZrO_2 to remove methylene orange using visible irradiation, reporting 83.7% removal.[28] Another alternative to improve the photocatalytic properties of ZrO_2 is the use of heterostructures. In this sense, due to their redox properties polyoxometalates (POM) are an interesting option to modify the ZrO_2 surface. POMs have empty d-orbitals, which become an electron acceptor region. This characteristic does not change upon doping, thus the presence of POMs might reduce the photocatalyst recombination process. Furthermore, the POM can increase the electronic transfer rates.[29,30] Sampurnam *et al.* reported the photocatalytic activity of hybrid ZrO_2 polyaniline–polyoxometalate ternary nanocomposites in the MB photodegradation under visible radiation.[31] Most of the reported studies have been carried out in a homogeneous phase. The main drawback of this application is the requirement of additional steps to recover the catalyst after the photocatalytic process. Different studies have demonstrated that immobilization (*e.g.* coatings, layers, and thin films) of POMs on adequate substances (*e.g.*, ZnO, TiO_2, and ZrO_2) is an appropriate method to obtain catalysts in a solid phase with a high surface area, porosity and, adequate optical properties to develop photocatalytic applications.[32,33] Diaz *et al.* reported a theoretical and experimental study of a TiO_2 photocatalysis modified with Anderson POMs (containing different central metals). The TiO_2/POM was more efficient in MB removal from water than bare TiO_2.[34,35] Most studies on photocatalytic POM applications include classical POMs (*e.g.*, Keggin, Dawson, and Lindquist). Furthermore, there are few reports about Anderson-type POM deposited on ZrO_2. The reported information indicates that a synergistic effect between the different POMs and ZrO_2 is present for this nanocomposite.[36–38] In this work, ZrO_2 thin films doped with Anderson-type MnPOM (ZrO_2/MnPOM) were synthesized and fully characterized and also the effect of the modifications on the photo-catalytic properties was studied. Finally, to support all the observed experimental results, DFT calculations were performed over a model system, to explain the observed catalytic activity.

2. Experimental

2.1 Materials

The following reagents were used without further purification: $Zr(NO_3)_4{\cdot}5H_2O$ (Sigma-Aldrich, 99%), urea (Sigma-Aldrich 99.5%), glucose (Sigma-Aldrich >99.5%), citric acid (Sigma-Aldrich >99.5%), $(NH_4)_6Mo_7O_{24}{\cdot}4H_2O$ (Merck, 99%), Mn $(NO_3)_2{\cdot}4H_2O$ (Sigma-Aldrich, 98%) and peroxymonosulfuric acid (Sigma-Aldrich 98%).

2.2. Synthesis of used compounds

ZrO_2 powder was synthesized by a sol–gel method.[39] First, 5 g (12.5 mmol) of $Zr(NO_3)_4{\cdot}5H_2O$ and 0.15 mg (2.5 mmol) of urea were mixed in water at 50 °C and pH = 5. Then, 2.1 g (11.7 mmol) of glucose (Sigma-Aldrich >99.5%) and 0.25 g (1.2 mmol) of citric acid (Sigma-Aldrich >99.5%) were added. This mixture was stirred for 4 days at 300 rpm until a homogeneous suspension was obtained. After that, the suspension was dried at 423 K for 12 hours in an oven. Finally, the sintering process was carried out at 873 K for 6 hours in a muffle. The mass ratio of the used reagents was Zr $(NO_3)_4{\cdot}5H_2O$: urea : glucose : citric acid (1 : 0.03 : 0.42 : 0.05). The yield of the process was 85%. The MnPOM was synthesized using 2.5 g (2.0 mmol) of $(NH_4)_6Mo_7O_{24}{\cdot}4H_2O$ (Merck, 99%) and 0.9 g (4.0 mmol) of $Mn(NO_3)_2{\cdot}4H_2O$ (Sigma-Aldrich, 98%), which were dissolved in 100 mL of distilled water by a co-precipitation method. The pH of this solution was adjusted to 4.0–5.0 using peroxomonosulfuric acid (H_2SO_5). The mixture was stirred at room temperature for 24 hours to allow for complete oxidation, followed by filtration and drying at 333.15 K for 24 hours. The yield of the process

was 90%. The synthesized MnPOM has the chemical formula $[MnMo_6O_{24}H_6]^{3-}$.[40]

2.3. Thin film deposition and characterization

We deposited ZrO_2 thin films using the Doctor Blade technique according to the procedure reported earlier.[41] The addition of the MnPOM over the ZrO_2 surface was carried out by a chemisorption process. Therefore, the thin films were immersed in a MnPOM suspension of 0.5 g (0.042 mmol) MnPOM in 100 mL of distilled water for 24 hours at 25 °C and stirring at 100 rpm. Then, the modified thin films were cleaned with distilled water and dried at 333.15 K. To ensure proper adherence of the nanoparticles to the thin films, a thermal treatment was performed in an oven at 523 K for 30 minutes. The obtained samples were characterized by UV-vis reflectance diffuse (ERS), FT-IR, SEM and EDX assay.

2.4. Adsorption and photocatalytic reactions

In the kinetic adsorption study, the thin films were immersed in a batch reactor (100 mL) with a solution of MB (10 mg L^{-1}). The system was stirred in darkness and the adsorption process was monitored by UV-vis spectrophotometry (at λ = 665 nm) until the adsorption/desorption equilibrium was reached. The process was carried out at different MB concentrations (20, 30, 40, 50 and 60 mg L^{-1}). In the photocatalytic test, after the adsorption/desorption equilibrium was reached, the system was irradiated with a UV tubular lamp manufactured by PHILIPS® (arc length 161 mm, tube diameter 16 mm, 7 W, 15 μW cm^{-2} at 1 m, emission maximum of 260 nm). The photocatalytic process was monitored by UV-vis spectrophotometry (at λ = 665 nm) every 20 minutes. Finally, the Langmuir–Hinshelwood (L–H) kinetic model was used to describe the photocatalytic process.

2.5. Computational details

Density functional (DFT) and time-dependent DFT (TDDFT) calculations were performed using the Amsterdam density functional package (ADF 2019.01) using the zeroth order regular approximation (ZORA) Hamiltonian with scalar corrections.[42,43] Slater type orbitals (STO) basis set using triple-ζ accuracy[44] with a single polarization function was employed (TZP). All optimizations were performed using analytical energy gradient techniques and the generalized gradient approximation (GGA) method with nonlocal exchange and correlation corrections within the BP86 functional.[45,46] The conductor-like screening model (COSMO) was used to model water as a solvent. Furthermore, to study the stability of ZrO_2/MnPOM, the Morokuma–Ziegler bonding energy decomposition analysis[43,47,48] was carried out. In this scheme, the interaction energy, ΔE_{Int}, is divided into the ΔE_{elec} + ΔE_{Pauli} + ΔE_{orb} + ΔE_{disp} components. (i) ΔE_{elec} can be related to the classical electrostatic interaction, calculated by superposition of the unperturbed fragment densities of the molecular geometry; (ii) ΔE_{Pauli}, represents the repulsive interactions between the fragments, as two electrons with the same quantum numbers cannot occupy the same region in the space and (iii) ΔE_{orb} is the stabilizing orbital interaction term.[49]

3. Results and discussion

3.1. FTIR characterization of thin films

Fig. 1 shows the FTIR spectra of the bare ZrO_2 and ZrO_2/MnPOM thin films. The band located at 3000–4000 cm^{-1} corresponds to –OH bond stretching of the film surface adsorbed water molecules. Also, the signal located at 1630 cm^{-1} corresponds to the bending of water –OH.[50–52] The signal located at 2380 cm^{-1} can be assigned to the Zr–OH bond stretching as previously reported.[53,54] The bare ZrO_2 spectrum shows a broad band at 660 cm^{-1}. This peak can be assigned to the stretching of the Zr–O bond.[54,55] The peak located at 1414 cm^{-1} is assigned to the nitrates from the precursor used during the POM's synthesis.[56–59] The peaks located between 1000 cm^{-1}–500 cm^{-1} are associated with the vibration of the MnPOM bonds. The characteristic signals located at 980 cm^{-1}; 660 cm^{-1} and 560 cm^{-1} are assigned to both symmetric and anti-asymmetric stretching bands of Mo–O–Mo bonds, which correspond to MnPOM. The signal located at 815 cm^{-1} is assigned to the stretching of the Mn–O bond, while the band located at 949 cm^{-1} is attributed to the bending of the Mn–OH bond. Finally, the peak located at 848 cm^{-1} is assigned to the bending of the Mn–O bond.[60,61]

3.2. Morphological characterization of thin films

The catalytic activity of any material is highly dependent on the shape, size, and size distribution of the particles. The morphological characteristics of ZrO_2 thin films are an important result before the development of catalytic applications. Fig. 2(a) shows SEM images of the thin films synthesized in this work. The bare ZrO_2 thin films consist of non-uniform microcrystals. In some regions, agglomerates can be observed; additionally, the SEM image shows holes in the ZrO_2 film.

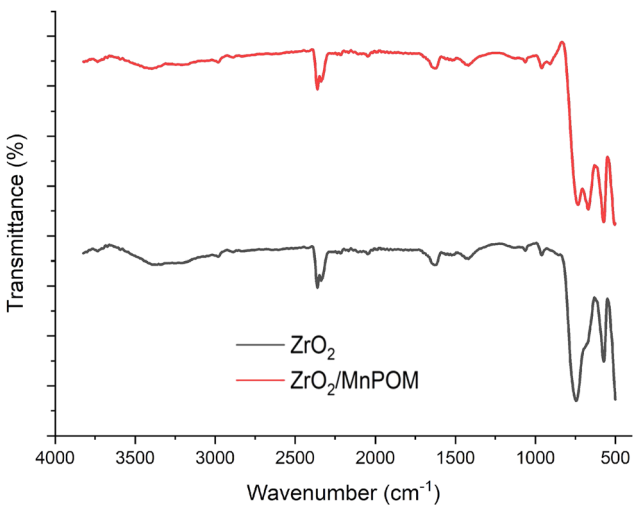

Fig. 1 FT-IR spectra of the bare ZrO_2 and ZrO_2/MnPOM thin films.

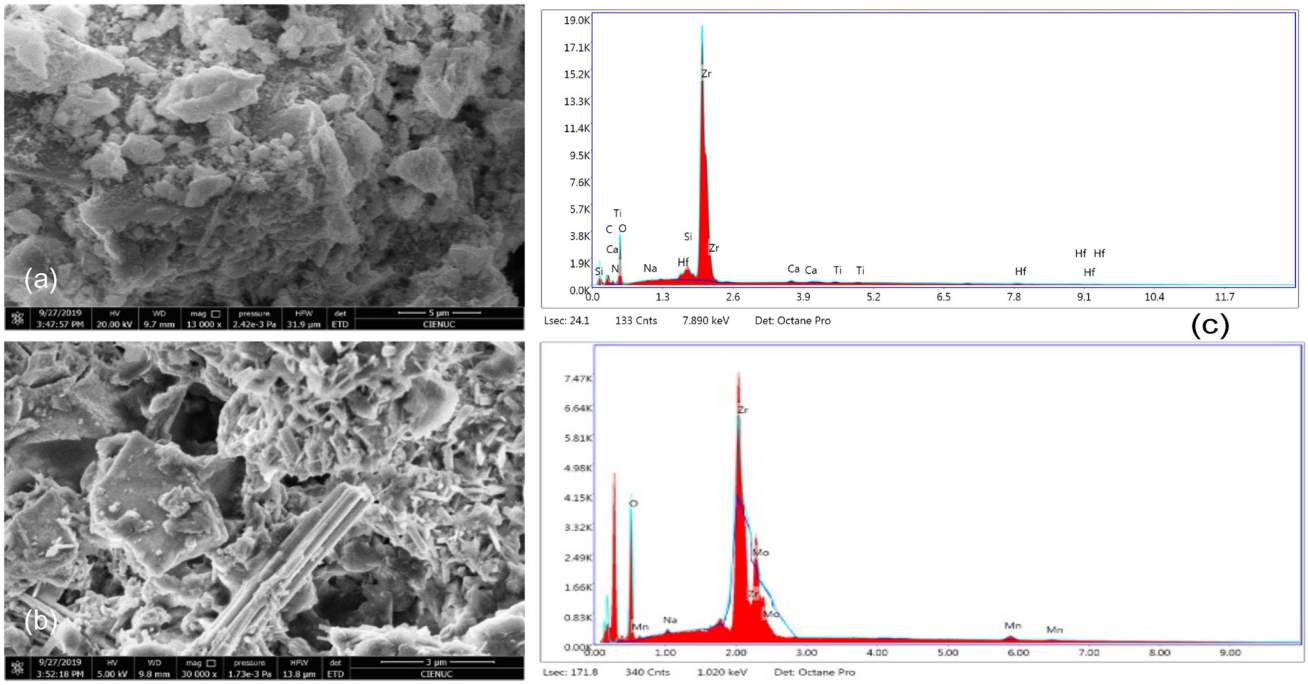

Fig. 2 SEM images of (a) ZrO_2, (b) ZrO_2/MnPOM thin films, and (c) EDX images of ZrO_2/MnPOM thin films.

This result is consistent with other reports on the use of the sol–gel synthesis method for ZrO_2 films.[49] After surface modification, the agglomeration increased and, the surface showed laminated agglomerates. These results could be beneficial for photocatalytic application, as photogenerated charge pairs can be separated between particles within agglomerates, reducing the recombination rates.[50] Fig. 2(b) shows the EDX assay for ZrO_2 and ZrO_2/MnPOM thin films, and Table 1 lists the elemental composition of the analyzed thin films. The shown result is in agreement with a 12% MnPOM chemisorption, as previously reported for similar modified materials.[50]

3.3. Optical thin film characterization

Fig. 3(a) shows UV-vis DRS of bare ZrO_2 and ZrO_2/MnPOM thin films. The bare ZrO_2 did not show any signal in the visible electromagnetic spectrum, this is in concordance with its higher energy band gap value. The signal in the spectrum (333 nm) corresponds to an electronic excitation from the valence band to the conduction band of the semiconductor due to the charge transfer transition O^{2-} ($2P \rightarrow Zr\ (A_{1g})$).[42] The ZrO_2/MnPOM thin film shows a red-shift in the optical activity with signals between (450 nm–590 nm) and (600–800 nm). This result suggests that ZrO_2/MnPOM can absorb visible radiation, improving the optical properties compared with the bare semiconductor. Fig. 1(b) shows the Kubelka–Munk function for the data shown in Fig. 1(a). The band gap (E_g) of catalysts can be calculated from this figure.[44,50] Thus, the bare ZrO_2 has an E_g value of 4.02 eV. This transition can be attributed to the structural extrinsic states due to particle size, surface defects, or traps of the material.[42,43] The E_g value reported for ZrO_2 is in the range of 3.5–5.1 eV, depending on the synthesis technique, thus our data are in agreement with those reported previously.[45,46] The ZrO_2/MnPOM shows an E_g value of 3.70 eV, this reduction in the energy transition can be associated with ligand-to-metal charge transfer (LMCT) that involves the Anderson-type POM structure.[48] This observed change in the UV-vis spectrum might affect the photocatalytic properties of the material.

Table 1 EDX results of the synthesized thin films

Thin film	% Zr	% O	% Mo	% Mn
ZrO_2	69.90	25.62	—	—
ZrO_2/MnPOM	55.19	24.84	10.62	7.65

3.4. Isothermal adsorption study

An important step before the photodegradation process of the pollutant is to reach the adsorption–desorption equilibrium state. This process is not commonly studied during photocatalytic activity studies. However, Zr-based sorbents have been known for their removal capacity of different pollutants.[62] In this work, we studied the removal of MB on bare ZrO_2 and ZrO_2/MnPOM thin films. We applied the isothermal models of Langmuir (1), Freundlich (2), Temkin (3) and Dubinin–Radushkevich (4) according to:[59,60]

$$q_e = \frac{q_m K_L C_e}{1 + K_L C_e} \quad (1)$$

$$q_e = K_F C_e^{1/n} \quad (2)$$

$$q_e = B_T \ln(A_T C_e) \quad (3)$$

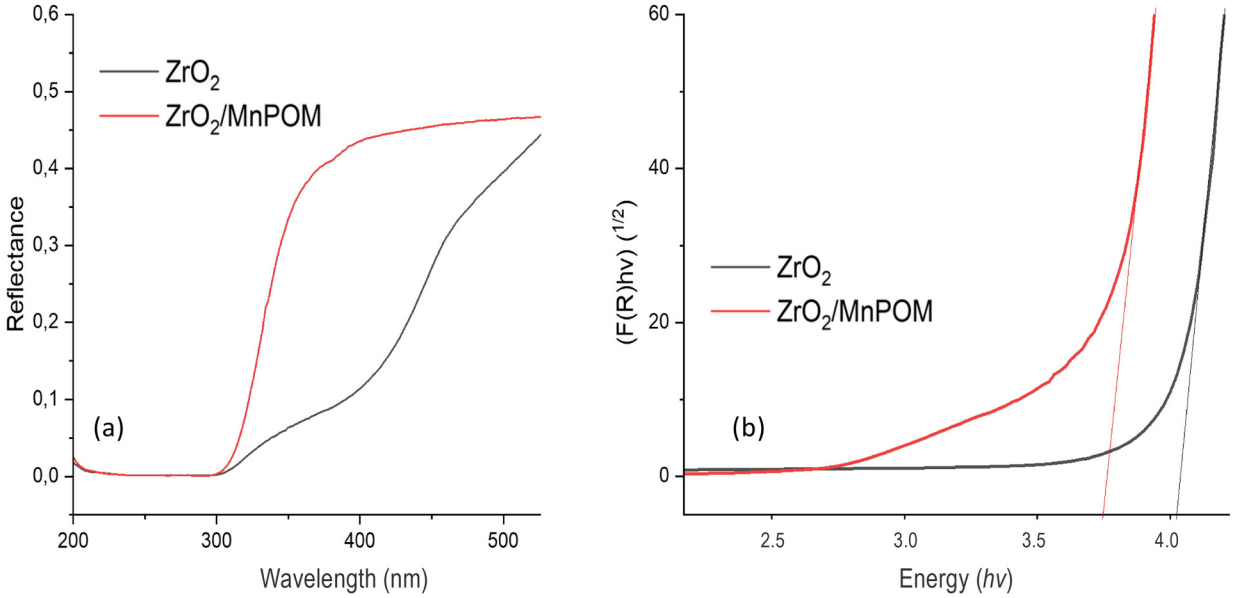

Fig. 3 (a) Diffuse reflectance spectra of thin films (b) Kubelka–Munk function and E_g value estimation.

$$q_e = q_m e^{-\beta\varepsilon^2}; \quad \varepsilon = RT\ln\left(1+\frac{1}{C_e}\right) \tag{4}$$

where C_e is the MB concentration (mg L^{-1}), q_e is the MB adsorbed on the catalyst (mg g^{-1}) in the adsorption/desorption equilibrium state, q_e is the maximum adsorption capacity, K_L is the Langmuir constant, K_F and n represent the intensity and the maximum adsorption capacity of Freundlich isotherm, respectively. B and K_T are the constants of the Temkin isotherm model and quantify the heat and the binding energy of the adsorption, respectively. Finally, the parameter β (mol^2 kJ^{-2}) is the Dubinin–Radushkevich constant, ε relates the Polanyi potential with the C_e and the saturation capacity of the catalyst (q_m).[61] Furthermore, we used the correlation coefficient (R^2) and the average relative error (ARE) to determine a suitable fitting:

$$\mathrm{ARE} = \frac{100}{n}\sum_{i=1}^{n}\frac{|q_e - q_f|}{q_e} \tag{5}$$

where q_e is the experimental value, q_f is the fitting value and n is the total of data.[62] Fig. 4 shows the isothermal fitting results and Table 2 lists the physical–chemical parameters of the fitting.

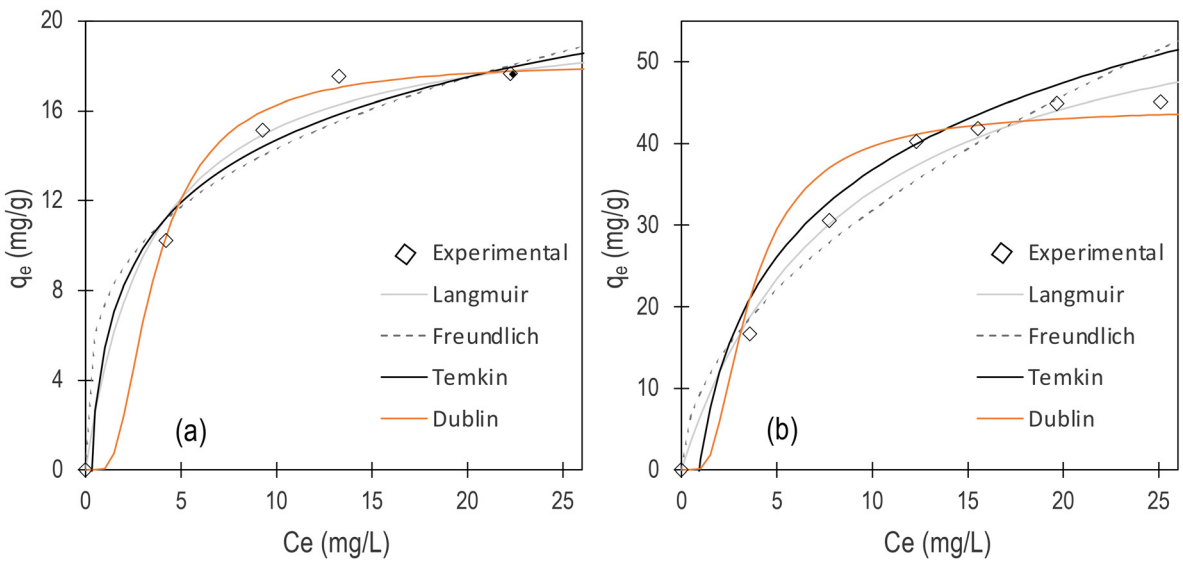

Fig. 4 Isothermal fitting results for the thin films of (a) ZrO_2 and (b) ZrO_2/MnPOM.

Table 2 Physical–chemical fitting results of the isothermal models

Isothermal model	Parameter	ZrO_2	ZrO_2/MnPOM
Freundlich	K_F (mg g^{-1})/(mg $L^{-1})^n$	7.37	1.90
	n	3.46	1.90
	R^2	0.865	0.925
	ARE (%)	8.5	8.6
Langmuir	q_m (mg g^{-1})	20.57	62.89
	K_L (L mg^{-1})	0.285	0.118
	R^2	0.995	0.977
	ARE (%)	3.4	4.9
Temkin	B_T	4.02	15.4
	A_T	3.84	1.09
	R^2	0.892	0.963
	ARE (%)	5.3	9.5
Dubinin–Radushkevich	β (mol^2 kJ^{-2}) × 10^{-6}	2.1	2.8
	q_m (mg g^{-1})	18.17	44.35
	R^2	0.984	0.970
	ARE (%)	4.3	9.2

The experimental data show an L-shaped isotherm indicating that the MB adsorption process has a strong competition between the water molecules and/or other molecules containing metal–oxygen (M–O) bonds for the active sites on the ZrO_2 surface.[60] This behavior has been previously reported for other semiconductors (*e.g.*, TiO_2, ZnO).[32,63] According to the results listed in Table 2, the Langmuir model adequately describes the ZrO_2 thin-film adsorption data (higher R^2 and smaller ARE), indicating a monolayer adsorption. This may indicate that the adsorption takes place at specific sites and that all the adsorption sites have equal affinity for the adsorbate. It might be further assumed that the adsorption on one site does not influence the adsorption on an adjacent site.[64] However, after the modification of the semiconductor by chemisorption of MnPOM, it is observed that the monolayer behavior adsorption of the MB changes to a multilayer adsorption (on the surface of ZrO_2/MnPOM).[65] Therefore, Langmuir's kinetic coefficients were higher for ZrO_2/MnPOM than for bare ZrO_2, suggesting a higher affinity for MB ions in the solution on ZrO_2/MnPOM than for bare ZrO_2 thin films. This behavior could be due to the interaction between POM metal–oxygen anion nanoclusters and the MB molecules.[66]

3.5. Kinetic adsorption study

To model the kinetic data, two models were applied: pseudo-first-order (6) and, pseudo-second-order (7), according to these equations:

$$\ln (q_t - q_e) = \ln(q_e) - k_1 t \quad (6)$$

$$\frac{t}{q_t} = \frac{1}{k_2 {q_e}^2} + \frac{t}{q_e} \quad (7)$$

where q_t is the MB adsorbed on the catalyst's surface (mg g^{-1}). q_e is the maximum adsorption capacity (mg g^{-1}), and k_1 (min^{-1}) and, k_2 (g mg^{-1} min^{-1}) are the rate constants to the pseudo-first and pseudo-second order, respectively. Fig. 5 shows the kinetic fitting of MB adsorption on the catalyst's thin films and Table 3 lists the physical chemical parameters of the fitting.

Recently, adsorption kinetics has been a relevant part of understanding the sorption processes, particularly in water treatment processes. However, it is notable that these processes have been less frequent and less explored in photocatalytic applications. The kinetic mechanism of MB adsorption in the catalysts can be studied indirectly using the kinetic models mentioned above. Results show that thin films reach the adsorption/desorption equilibrium after (25 min to

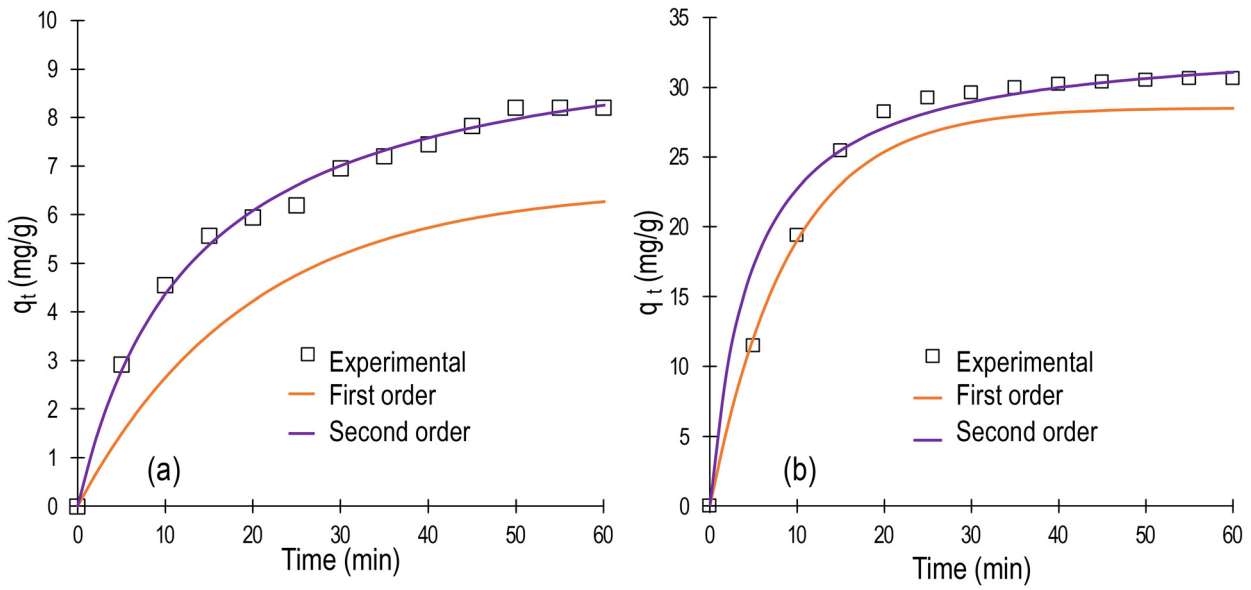

Fig. 5 Kinetic fitting results of MB adsorption on both thin films: (a) ZrO_2 and (b) ZrO_2/MnPOM.

Table 3 Kinetic adsorption model fitting results for MB adsorption onto thin films

Model	Parameters	ZrO_2	ZrO_2/MnPOM
1st order	q_e (mg g^{-1})	28.3	34.8
	k_1 (min^{-1})	0.109	0.151
	R^2	0.978	0.991
	ARE (%)	5.8	3.3
2nd order	q_e (mg g^{-1})	28.5	33.5
	k_2 (g mg^{-1} min^{-1}) × 10^{-3}	0.150	0.209
	R^2	0.983	0.996
	ARE (%)	6.5	2.5

30 min).[67] The bare ZrO_2 thin film showed a lower removal capacity (~8%) than ZrO_2/MnPOM thin films (~29%), indicating a greater affinity of MB for ZrO_2/MnPOM than for bare ZrO_2. This might be due to the anionic properties of the POMs assisting the sorption of the cationic dyes (*e.g.*, MB).[29,65] The pseudo-second-order model was appropriate to describe the experimental data for the adsorption process (higher R^2 and smaller ARE, see Table 3). During MB adsorption on the thin film surface, chemisorption is considered as the main chemical interaction. The adsorption rate is proportional to the MB concentration and behaves similarly to the first-order kinetics in terms of its adsorption rate. In this context, effective electrostatic interactions play a significant role in the adsorption phenomenon. The k_2 values of the pseudo-second-order model show a larger value for ZrO_2/MnPOM compared to bare ZrO_2, indicating that both the adsorption capacity and the adsorption rate increased after the modification of the ZrO_2 thin films.

3.6. Photocatalytic study

In the kinetic degradation study, the Langmuir–Hinshelwood model was applied[68] as shown below.

$$\ln [MB]_t = \ln [MB]_0 - k_{ap}(t) \quad (8)$$

where $[MB]_t$ is the MB concentration as a function of time irradiation; (t) is the time irradiation and the k_{ap} is the rate constant of the process (min^{-1}). Fig. 6 shows the MB concentration decay under UV irradiation onto bare ZrO_2 and ZrO_2/MnPOM thin films. Bare ZrO_2 thin films reached 18% of MB photodegradation, whereas ZrO_2/MnPOM thin films reached 43% of MB photodegradation. The Langmuir–Hinshelwood model fitting shows that bare ZrO_2 thin films have a k_{ap} value (2×10^{-3} min^{-1}) smaller than ZrO_2/MnPOM (5.4×10^{-3} min^{-1}). Therefore, the adsorbed POM could act as an electron scavenger both on the surface and in the bulk of the material, reducing the recombination rate, and thus, increasing the photocatalytic properties.[32,69] The previously shown band gap reduction observed for ZrO_2/MnPOM could be responsible for the increased photocatalytic activity. Similar results have been reported before for ZrO_2 modified with POMs, as shown in Table 4.[32,50,70]

The recyclability of the catalysts is an important parameter for developing photocatalytic applications. Fig. 7a shows the

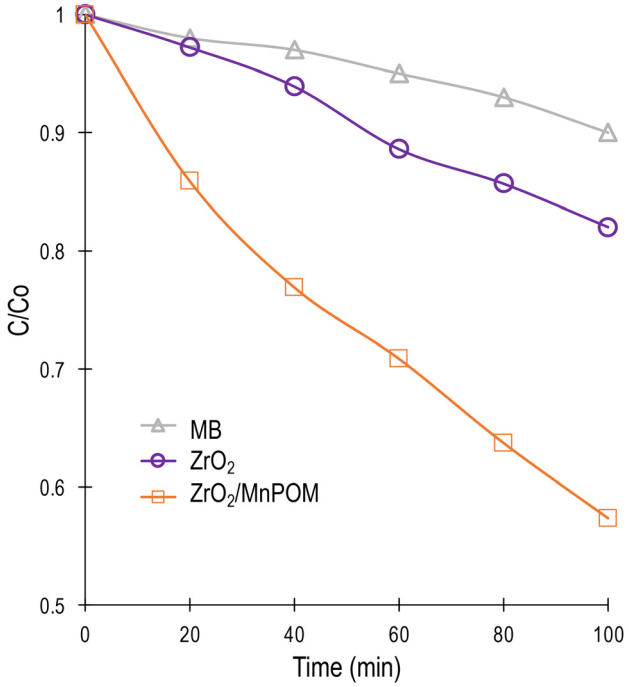

Fig. 6 MB concentration decay under UV irradiation for free MB and onto bare ZrO_2 and ZrO_2/MnPOM thin films.

Table 4 Photocatalytic efficiency of different systems under UV irradiation

Semiconductor	Pollutant/ irradiation time	Degradation efficiency (%)	Ref.
ZnO-Ag	MB/180 min	35	71
BCTi[b]/powder	MB/180 min	90	72
CoPOM/TiO_2	MB/300 min	50	73
SnO_2/Fe	RB[a]/180 min	55	74
ZrO_2/MnPOM	MB/100 min	43	This work

[a] Thin films. [b] Graphene oxide.

results of the stability tests for bare ZrO_2 and ZrO_2/MnPOM thin films. The ZrO_2 films did not change significantly their MB adsorption capacity even after the third cycle, suggesting that the thin film deposition method was suitable. Fig. 7 shows that the MB adsorbed amount onto recycled ZrO_2/MnPOM thin films reduced gradually after each photocatalytic cycle from 28% to 15%. Furthermore, the same trend was observed in the photocatalytic test. Fig. 7b shows a slight decrease in photocatalytic degradation after three cycles from 43% to 31%. The loss in photocatalytic activity might be associated with the amount of the catalyst diminution through the cycles. This result is similar to the one reported by Tang *et al.*, where they reported the obstruction of the adsorption by surface residuals and the mass loss during catalyst recovery in the bisphenol A photodegradation using POMs/TiO_2 photocatalysts after 4 photocatalytic cycles.[75]

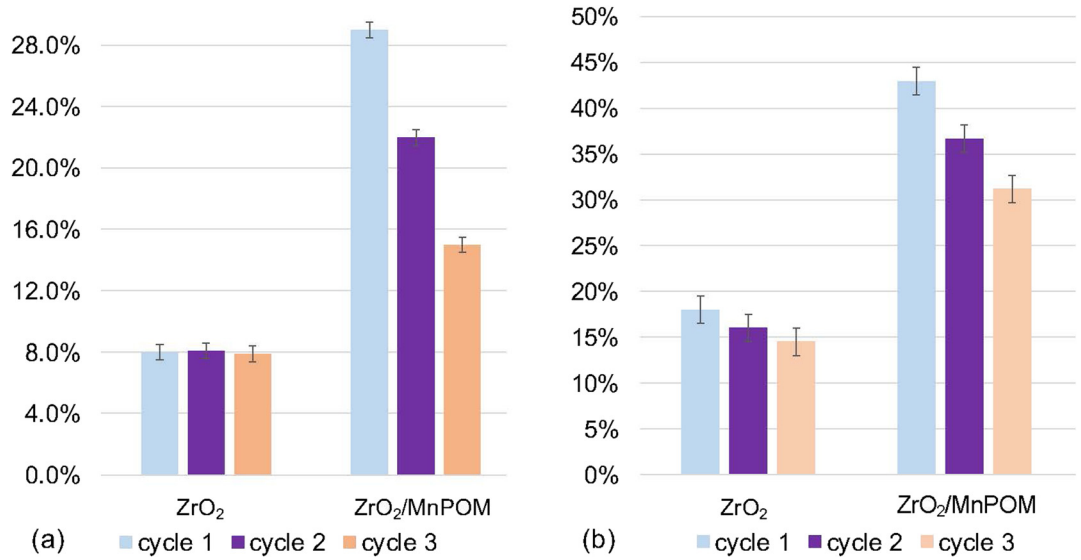

Fig. 7 Recyclability tests for photocatalytic degradation of MB onto ZrO_2 and ZrO_2/MnPOM thin films. (a) Adsorption (b) photocatalytic degradation.

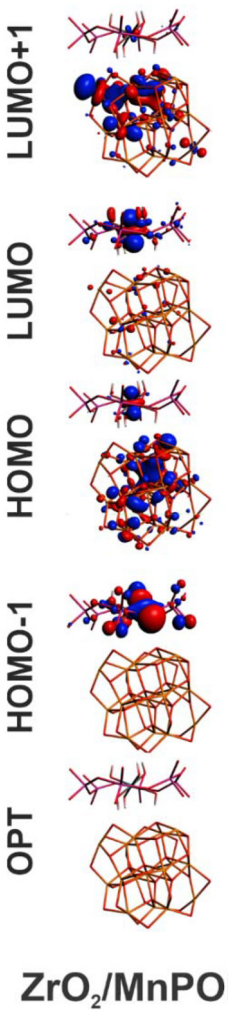

Fig. 8 Frontier molecular orbitals for the ZrO_2/MnPOM.

3.7. Computational modeling

It has been previously shown that ZrO_2/CrPOM has a 43% degradation under UV irradiation.[50] In this report, a slightly smaller degradation capability was obtained for ZrO_2/MnPOM. These slight observed differences can be supported with the FMO localization, the global reactivity indexes and the EDA analysis. Therefore, a reduced model considering a ZrO_2 nanoparticle representation and one MnPOM was considered. The EDA analysis shows similar results to those previously reported. Furthermore, it is observed that the most active compounds and Mn, have the largest stabilization energy on the ZrO_2 surface. This corroborates that the most stable molecule has the best catalytic conversion over MB. The observed stabilization is mostly due to the electrostatic contribution, which correlates with the large charge of the studied POM. As shown in Fig. 8, the HOMO and the LUMO show large contributions to the d_{z^2} orbital. The reactivity indexes show the MnPOM has similar reactivity in terms of chemical potential and chemical hardness than the CrPOM (which shows the best photocatalytic activity), see Table 5. Also, MnPOM shows a large value of electrophilicity compared to the CoPOM and CuPOM.[50]

Finally, to provide a better rationalization of the photocatalytic activity for the MnPOM, TD-DFT calculations were performed. As described before, due to the addition of the MnPOM to the, there is observed an LMCT between the nanoparticle and POM, see Table 6. This transition involves orbitals that are located over the ZrO_2 nanoparticle towards the MnPOM nanoparticle. Furthermore, larger energy transitions have the opposite direction (from the MnPOM towards the ZrO_2 nanoparticle), data not shown. This charge separation induced by the presence of the MnPOM in the structure would explain the enhanced photocatalytic activity.

Table 5 Bonding energy decomposition analysis Morokuma–Ziegler EDA, HOMO, LUMO, GAP and reactivity indexes in eV

	ΔE_{Pauli}	ΔE_{orb}	ΔE_{elect}	ΔE_{disp}	ΔE_{tot}	HOMO	LUMO	GAP	μ	η	ω
MnPOM	14.26	−40.10 (36)	−70.64 (63)	−0.42	−96.90	−5.39	−3.55	1.84	−4.47	0.92	10.84

Table 6 Theoretical TD-DFT transitions observed in the UV-vis spectra. The extinction coefficient (f), orbitals involved and the oscillator strength are also reported for each transition

Compound	Λ_{th}	f	Contribution			%
ZrO_2/MnPOM	330	1.20×10^{-3}	HOMO−1	→	LUMO	89

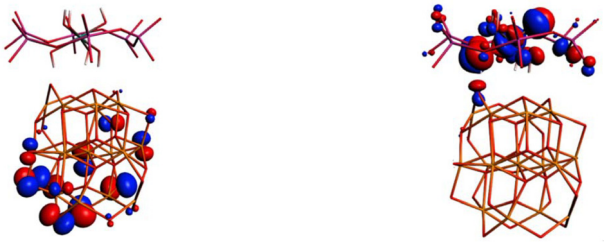

4. Conclusions

A novel photocatalytic system based on ZrO_2/POMs was synthesized and characterized, exploring the incorporation of manganese (Mn^{3+}) as a transition metal within the molecular structure of POMs. Optical results show a red shift in the optical activity of the MnPOM-modified material, the band gap value was lower for ZrO_2 (3.70 eV) than the band gap value of ZrO_2/MnPOM (3.70 eV). Modeling of MB adsorption on thin films revealed that the Langmuir model was suitable to describe the adsorption process on both materials. Modified ZrO_2 thin films were more efficient in the photocatalytic degradation of MB. Specifically bare ZrO_2 thin films show a k_{ap} value (2×10^{-3} min^{-1}) smaller than that of ZrO_2/MnPOM (5.4×10^{-3} min^{-1}). Results showed a significant improvement in the adsorption capacity after modification of ZrO_2 with MnPOM, providing a positive effect on photochemical, photophysical and photocatalytic properties. This increase in efficiency can be attributed to improvement in the adsorption capacity and optical properties of the material after modification with MnPOM. Furthermore, DFT calculations suggested that charge separation induced due to the presence of MnPOM in the structure would explain the enhanced photocatalytic activity.

Data availability

The data supporting this article have been included within the main document; no additional data are presented.

Conflicts of interest

There are no conflicts to declare.

Acknowledgements

C. D.-U., W. V., would like to thank Universidad del Atlántico. The authors would like to acknowledge ANID/FONDAP/1523A0006; FONDECYT 1241917, 1231194, the Anillos de Ciencia y Tecnología ACT210057 and ANID Postdoctoral 3240414.

References

1 K.-E. Norrman, World Population Growth: A Once and Future Global Concern, *World*, 2023, **4**, 684–697, DOI: **10.3390/world4040043**.
2 G. Shaddick, M. L. Thomas, P. Mudu, G. Ruggeri and S. Gumy, Half the world's population are exposed to increasing air pollution, *npj Clim. Atmos. Sci.*, 2020, **3**, 23, DOI: **10.1038/s41612-020-0124-2**.
3 B. J. Singh, A. Chakraborty and R. Sehgal, A systematic review of industrial wastewater management: Evaluating challenges and enablers, *J. Environ. Manage.*, 2023, **348**, 119230, DOI: **10.1016/j.jenvman.2023.119230**.
4 D. Dutta, S. Arya and S. Kumar, Industrial wastewater treatment: Current trends, bottlenecks, and best practices, *Chemosphere*, 2021, **285**, 131245, DOI: **10.1016/j.chemosphere.2021.131245**.
5 K. Fouad, M. Bassyouni, M. G. Alalm and M. Y. Saleh, Recent developments in recalcitrant organic pollutants degradation using immobilized photocatalysts, *Appl. Phys. A*, 2021, **127**, 612, DOI: **10.1007/s00339-021-04724-1**.
6 G. Balasundaram, R. Banu, S. Varjani, A. A. Kazmi and V. K. Tyagi, Recalcitrant compounds formation, their toxicity, and mitigation: Key issues in biomass pretreatment

and anaerobic digestion, *Chemosphere*, 2022, **291**, 132930, DOI: 10.1016/j.chemosphere.2021.132930.

7 P. O. Oladoye, T. O. Ajiboye, E. O. Omotola and O. J. Oyewola, Methylene blue dye: Toxicity and potential elimination technology from wastewater, *Results Eng.*, 2022, **16**, 100678, DOI: 10.1016/j.rineng.2022.100678.

8 M. Ibrahim, M. H. Nawaz, P. R. Rout, J.-W. Lim, B. Mainali and M. K. Shahid, Advances in Produced Water Treatment Technologies: An In-Depth Exploration with an Emphasis on Membrane-Based Systems and Future Perspectives, *Water*, 2023, **15**, 2980, DOI: 10.3390/w15162980.

9 U. Hübner, S. Spahr, H. Lutze, A. Wieland, S. Rüting, W. Gernjak and J. Wenk, Advanced oxidation processes for water and wastewater treatment – Guidance for systematic future research, *Heliyon*, 2024, **10**, e30402, DOI: 10.1016/j.heliyon.2024.e30402.

10 H. Sies, V. V. Belousov, N. S. Chandel, M. J. Davies, D. P. Jones, G. E. Mann, M. P. Murphy, M. Yamamoto and C. Winterbourn, Defining roles of specific reactive oxygen species (ROS) in cell biology and physiology, *Nat. Rev. Mol. Cell Biol.*, 2022, **23**, 499–515, DOI: 10.1038/s41580-022-00456-z.

11 S. Khan, M. Sayed, M. Sohail, L. A. Shah and M. A. Raja, Advanced Oxidation and Reduction Processes, in *Advances in Water Purification Techniques*, Elsevier, 2019, pp. 135–164. DOI: 10.1016/B978-0-12-814790-0.00006-5.

12 J. J. Rueda-Marquez, I. Levchuk, P. Fernández Ibañez and M. Sillanpää, A critical review on application of photocatalysis for toxicity reduction of real wastewaters, *J. Cleaner Prod.*, 2020, **258**, 120694, DOI: 10.1016/j.jclepro.2020.120694.

13 H. Wang, X. Li, X. Zhao, C. Li, X. Song, P. Zhang, P. Huo and X. Li, A review on heterogeneous photocatalysis for environmental remediation: From semiconductors to modification strategies, *Chin. J. Catal.*, 2022, **43**, 178–214, DOI: 10.1016/S1872-2067(21)63910-4.

14 W. Vallejo, A. Cantillo and C. Díaz-Uribe, Methylene Blue Photodegradation under Visible Irradiation on Ag-Doped ZnO Thin Films, *Int. J. Photoenergy*, 2020, **2020**, 1–11, DOI: 10.1155/2020/1627498.

15 W. Vallejo, C. E. Diaz-Uribe and F. Duran, Kinetic and Thermodynamic Study of Methylene Blue Adsorption on TiO2 and ZnO Thin Films, *Materials*, 2023, **16**, 4434, DOI: 10.3390/ma16124434.

16 N. Kumari, S. Sareen, M. Verma, S. Sharma, A. Sharma, H. S. Sohal, S. K. Mehta, J. Park and V. Mutreja, Zirconia-based nanomaterials: recent developments in synthesis and applications, *Nanoscale Adv.*, 2022, **4**, 4210–4236, DOI: 10.1039/D2NA00367H.

17 J. Rengaswamy, R. Sathasivam, P. Chellaia Muthammal, A. Davix and X. Durai, Structural Optical Thermal Magnetic Properties of Zirconia Nano-rods and their Photocatalytic and Antimicrobial Properties, *J. Water Environ. Nanotechnol.*, 2021, **6**(3), 252–264, DOI: 10.22090/jwent.2021.03.006.

18 D. Zhang and F. Zeng, Structural, photochemical and photocatalytic properties of zirconium oxide doped TiO2 nanocrystallites, *Appl. Surf. Sci.*, 2010, **257**, 867–871, DOI: 10.1016/j.apsusc.2010.07.083.

19 R. Biju, R. Ravikumar, J. R. V. Raghavan and C. R. Indulal, Nanocomposite of zinc zirconia for better degradation of an organic dye, *Bull. Mater. Sci.*, 2022, **45**, 180, DOI: 10.1007/s12034-022-02753-x.

20 E. M. S. Aldeen, A. A. Jalil, R. S. Mim, A. Alhebshi, N. S. Hassan and R. Saravanan, Altered zirconium dioxide based photocatalyst for enhancement of organic pollutants degradation: A review, *Chemosphere*, 2022, **304**, 135349, DOI: 10.1016/j.chemosphere.2022.135349.

21 H. Singh, Sunaina, K. K. Yadav, V. K. Bajpai and M. Jha, Tuning the bandgap of m-ZrO2 by incorporation of copper nanoparticles into visible region for the treatment of organic pollutants, *Mater. Res. Bull.*, 2020, **123**, 110698, DOI: 10.1016/j.materresbull.2019.110698.

22 L. Qi, M. Wang, J. Xue, Q. Zhang, F. Chen, Q. Liu, W. Li and X. Li, Simultaneous Tuning Band Gaps of Cu_2 O and TiO_2 to Form S-Scheme Hetero-Photocatalyst, *Chem. – Eur. J.*, 2021, **27**, 14638–14644, DOI: 10.1002/chem.202102120.

23 M. Niu, K. Sui, X. Wu, D. Cao and C. Liu, GaAs quantum dot/TiO2 heterojunction for visible-light photocatalytic hydrogen evolution: promotion of oxygen vacancy, *Adv. Compos. Hybrid Mater.*, 2022, **5**, 450–460, DOI: 10.1007/s42114-021-00296-z.

24 E. S. Agorku, A. T. Kuvarega, B. B. Mamba, A. C. Pandey and A. K. Mishra, Enhanced visible-light photocatalytic activity of multi-elements-doped ZrO2 for degradation of indigo carmine, *J. Rare Earths*, 2015, **33**, 498–506, DOI: 10.1016/S1002-0721(14)60447-6.

25 S. N. Basahel, T. T. Ali, M. Mokhtar and K. Narasimharao, Influence of crystal structure of nanosized ZrO2 on photocatalytic degradation of methyl orange, *Nanoscale Res. Lett.*, 2015, **10**, 73, DOI: 10.1186/s11671-015-0780-z.

26 F. Boran and M. Okutan, Synthesis optimization of ZrO2 nanostructures for photocatalytic applications, *Turk. J. Chem.*, 2023, **47**, 448–464, DOI: 10.55730/1300-0527.3551.

27 H. Chen, G. Jiang, T. Jiang, L. Li, Y. Liu, Q. Huang and W. Chen, Preparation of Mn-doped ZrO2/TiO2 photocatalysts for efficient degradation of Rhodamine B, *MRS Commun.*, 2015, **5**, 525–531, DOI: 10.1557/mrc.2015.59.

28 C. V. Reddy, I. N. Reddy, B. Akkinepally, V. V. N. Harish, K. R. Reddy and S. Jaesool, Mn-doped ZrO2 nanoparticles prepared by a template-free method for electrochemical energy storage and abatement of dye degradation, *Ceram. Int.*, 2019, **45**, 15298–15306, DOI: 10.1016/j.ceramint.2019.05.020.

29 D. Carriazo, M. Addamo, G. Marcì, C. Martín, L. Palmisano and V. Rives, Tungstophosphoric acid supported on polycrystalline TiO2 for the photodegradation of 4-nitrophenol in aqueous solution and propan-2-ol in vapour phase, *Appl. Catal., A*, 2009, **356**, 172–179, DOI: 10.1016/j.apcata.2009.01.010.

30 E. López-Salinas, J. G. Hernández-Cortéz, M. A. Cortés-Jácome, J. Navarrete, M. E. Llanos, A. Vázquez,

H. Armendáriz and T. López, Skeletal isomerization of 1-butene on 12-tungstophosphoric acid supported on zirconia, *Appl. Catal., A*, 1998, **175**, 43–53, DOI: 10.1016/S0926-860X(98)00198-7.

31 S. Sampurnam, S. Muthamizh, S. Balachandran and V. Narayanan, Fabrication of hybrid polyaniline – Polyoxometalate decorated with ZrO2 ternary nanocomposites with excellent visible light driven photocatalytic performance, *J. Photochem. Photobiol., A*, 2023, **443**, 114844, DOI: 10.1016/j.jphotochem.2023.114844.

32 A. Sanguino, C. Diaz-Uribe, F. Duran, W. Vallejo, L. Guzman, D. Ruiz, E. Puello, C. Quiñones, E. Schott and X. Zarate, Photocatalytic Degradation of Methylene Blue under Visible Light Using TiO2 Thin Films Impregnated with Porphyrin and Anderson-Type Polyoxometalates (Cu and Zn), *Catalysts*, 2022, **12**, 1169, DOI: 10.3390/catal12101169.

33 S. Farhadi and M. Zaidi, Polyoxometalate–zirconia (POM/ZrO2) nanocomposite prepared by sol–gel process: A green and recyclable photocatalyst for efficient and selective aerobic oxidation of alcohols into aldehydes and ketones, *Appl. Catal., A*, 2009, **354**, 119–126, DOI: 10.1016/j.apcata.2008.11.024.

34 C. Diaz-Uribe, F. Duran, W. Vallejo, E. Puello, X. Zarate and E. Schott, Photocatalytic study of TiO2 thin films modified with Anderson-type polyoxometalates (Cr, Co and Ni): Experimental and DFT study, *Polyhedron*, 2023, **231**, 116253, DOI: 10.1016/j.poly.2022.116253.

35 F. Duran, C. Diaz-Uribe, W. Vallejo, A. Muñoz-Acevedo, E. Schott and X. Zarate, Adsorption and Photocatalytic Degradation of Methylene Blue on TiO_2 Thin Films Impregnated with Anderson-Evans Al-Polyoxometalates: Experimental and DFT Study, *ACS Omega*, 2023, **8**, 27284–27292, DOI: 10.1021/acsomega.3c02657.

36 P. Wu, Y. Wang, B. Huang and Z. Xiao, Anderson-type polyoxometalates: from structures to functions, *Nanoscale*, 2021, **13**, 7119–7133, DOI: 10.1039/D1NR00397F.

37 Q. Liu, T. Su, H. Zhang, W. Liao, W. Ren, Z. Zhu, K. Yang, C. Len, J. Yu, D. Zhao and H. Lü, Development of TiO2 catalyst based on Anderson-polyoxometalates for efficient visible-light-driven photocatalytic oxidative desulfurization, *Fuel*, 2023, **333**, 126286, DOI: 10.1016/j.fuel.2022.126286.

38 H. Salavati, N. Tavakkoli and M. Hosseinpoor, Preparation and characterization of polyphosphotungstate/ZrO2 nanocomposite and their sonocatalytic and photocatalytic activity under UV light illumination, *Ultrason. Sonochem.*, 2012, **19**, 546–553, DOI: 10.1016/j.ultsonch.2011.09.001.

39 E. Puello-Polo, E. Marquez and J. L. Brito, One-pot synthesis of Nb-modified Al_2O_3 support for NiMo hydrodesulfurization catalysts, *J. Sol-Gel Sci. Technol.*, 2018, **88**, 90–99, DOI: 10.1007/s10971-018-4792-x.

40 C. Yvon, A. Macdonell, S. Buchwald, A. J. Surman, N. Follet, J. Alex, D.-L. Long and L. Cronin, A collection of robust methodologies for the preparation of asymmetric hybrid Mn–Anderson polyoxometalates for multifunctional materials, *Chem. Sci.*, 2013, **4**, 3810–3817, DOI: 10.1039/C3SC51618K.

41 C. Quiñones, J. Ayala and W. Vallejo, Methylene blue photoelectrodegradation under UV irradiation on Au/Pd-modified TiO2 films, *Appl. Surf. Sci.*, 2010, **257**, 367–371, DOI: 10.1016/j.apsusc.2010.06.079.

42 E. Van Lenthe, E. J. Baerends and J. G. Snijders, Relativistic total energy using regular approximations, *J. Chem. Phys.*, 1994, **101**, 9783–9792, DOI: 10.1063/1.467943.

43 G. Te Velde, F. M. Bickelhaupt, E. J. Baerends, C. F. Guerra, S. J. A. Van Gisbergen, J. G. Snijders and T. Ziegler, Chemistry with ADF, *J. Comput. Chem.*, 2001, **22**, 931–967, DOI: 10.1002/jcc.1056.

44 J. G. Snijders, P. Vernooijs and E. J. Baerends, Roothaan-Hartree-Fock-Slater atomic wave functions, *At. Data Nucl. Data Tables*, 1981, **26**, 483–509, DOI: 10.1016/0092-640X(81)90004-8.

45 J. P. Perdew and W. Yue, Accurate and simple density functional for the electronic exchange energy: Generalized gradient approximation, *Phys. Rev. B:Condens. Matter Mater. Phys.*, 1986, **33**, 8800–8802, DOI: 10.1103/PhysRevB.33.8800.

46 A. D. Becke, Density-functional exchange-energy approximation with correct asymptotic behavior, *Phys. Rev. A*, 1988, **38**, 3098–3100, DOI: 10.1103/PhysRevA.38.3098.

47 T. Ziegler and A. Rauk, On the calculation of bonding energies by the Hartree Fock Slater method: I. The transition state method, *Theor. Chim. Acta*, 1977, **46**, 1–10, DOI: 10.1007/BF02401406.

48 T. Ziegler and A. Rauk, A theoretical study of the ethylene-metal bond in complexes between copper(1+), silver(1+), gold(1+), platinum(0) or platinum(2+) and ethylene, based on the Hartree-Fock-Slater transition-state method, *Inorg. Chem.*, 1979, **18**, 1558–1565, DOI: 10.1021/ic50196a034.

49 E. Schott, X. Zárate and R. Arratia-Pérez, Relativistic scalar and spin–orbit density functional calculations of the electronic structure, NICS index and ELF function of the [Re2(CO)8(μ-BiPh)2] and [Re2(CO)8(μ-BiPh2)2] clusters, *Polyhedron*, 2011, **30**, 846–850, DOI: 10.1016/j.poly.2010.12.022.

50 C. Diaz-Uribe, J. Florez, W. Vallejo, F. Duran, E. Puello, V. Roa, E. Schott and X. Zarate, Removal and photocatalytic degradation of methylene blue on ZrO2 thin films modified with Anderson-Polioxometalates (Cr3+, Co3+, Cu2+): An experimental and theoretical study, *J. Photochem. Photobiol., A*, 2024, **454**, 115689, DOI: 10.1016/j.jphotochem.2024.115689.

51 Y. Park, W. Kim, D. Monllor-Satoca, T. Tachikawa, T. Majima and W. Choi, Role of Interparticle Charge Transfers in Agglomerated Photocatalyst Nanoparticles: Demonstration in Aqueous Suspension of Dye-Sensitized TiO_2, *J. Phys. Chem. Lett.*, 2013, **4**, 189–194, DOI: 10.1021/jz301881d.

52 G.-Y. Guo, Y.-L. Chen and W.-J. Ying, Thermal, spectroscopic and X-ray diffractional analyses of zirconium hydroxides precipitated at low pH values, *Mater. Chem. Phys.*,

2004, **84**, 308–314, DOI: 10.1016/j.matchemphys.2003.10.006.

53 C. Diaz-Uribe, W. Vallejo and W. Ramos, Methylene blue photocatalytic mineralization under visible irradiation on TiO2 thin films doped with chromium, *Appl. Surf. Sci.*, 2014, **319**, 121–127, DOI: 10.1016/j.apsusc.2014.06.157.

54 B. Balraj, M. Arulmozhi, C. Siva and R. Krithikadevi, Synthesis, characterization and electrochemical analysis of hydrothermal synthesized AgO incorporated ZrO2 nanostructures, *J. Mater. Sci.: Mater. Electron.*, 2017, **28**, 5906–5912, DOI: 10.1007/s10854-016-6264-9.

55 N. C. Horti, M. D. Kamatagi, S. K. Nataraj, M. N. Wari and S. R. Inamdar, Structural and optical properties of zirconium oxide (ZrO_2) nanoparticles: effect of calcination temperature, *Nano Express*, 2020, **1**, 010022, DOI: 10.1088/2632-959X/ab8684.

56 M. E. M. Ali, S. M. Abdel Moniem, H. S. Ibrahim, N. S. Ammar, H. K. El-Kholly, A. G. El-Deen, M. K. Zahran and M. H. Helal, Production of zirconia materials from zircon for dye removal from wastewater, *Egypt. J. Chem.*, 2020, **63**, 515–523, DOI: 10.21608/ejchem.2019.13583.1838.

57 M. Abd El-Aal, R. T. Mogharbel, A. Ibrahim, N. Almutlaq, M. Sh Zoromba, A. F. Al-Hossainy and S. M. Ibrahim, Synthesis, characterization, and photosensitizer applications for dye-based on ZrO2- acriflavine nanocomposite thin film [ZrO2+ACF]C, *J. Mol. Struct.*, 2022, **1250**, 131827, DOI: 10.1016/j.molstruc.2021.131827.

58 S. Kumar, S. Bhunia and A. K. Ojha, Effect of calcination temperature on phase transformation, structural and optical properties of sol–gel derived ZrO2 nanostructures, *Phys. E*, 2015, **66**, 74–80, DOI: 10.1016/j.physe.2014.09.007.

59 J. M. E. Matos, F. M. Anjos Júnior, L. S. Cavalcante, V. Santos, S. H. Leal, L. S. Santos Júnior, M. R. M. C. Santos and E. Longo, Reflux synthesis and hydrothermal processing of ZrO2 nanopowders at low temperature, *Mater. Chem. Phys.*, 2009, **117**, 455–459, DOI: 10.1016/j.matchemphys.2009.06.024.

60 H. C. Madhusudhana, S. N. Shobhadevi, B. M. Nagabhushana, B. V. Chaluvaraju, M. V. Murugendrappa, R. Hari Krishna, H. Nagabhushana and N. R. Radeep, Effect of fuels on conductivity, dielectric and humidity sensing properties of ZrO_2 nanocrystals prepared by low temperature solution combustion method, *J. Asian Ceram. Soc.*, 2016, **4**, 309–318, DOI: 10.1016/j.jascer.2016.05.009.

61 H. A. Özbek, Synthesis and characterization of Anderson-Evans type polyoxometalates, antibacterial properties, *Turk. J. Chem.*, 2023, **47**, 742–748, DOI: 10.55730/1300-0527.3575.

62 C. Diaz-Uribe, L. Walteros, F. Duran, W. Vallejo and A. R. Romero Bohórquez, *Prosopis juliflora* Seed Waste as Biochar for the Removal of Blue Methylene: A Thermodynamic and Kinetic Study, *ACS Omega*, 2022, **7**, 42916–42925, DOI: 10.1021/acsomega.2c05007.

63 W. S. Al-Arjan, Zinc Oxide Nanoparticles and Their Application in Adsorption of Toxic Dye from Aqueous Solution, *Polymers*, 2022, **14**, 3086, DOI: 10.3390/polym14153086.

64 I. Langmuir, The Adsorption of Gases on Plane Surfaces of Glass, Mica and Platinum, *J. Am. Chem. Soc.*, 1918, **40**, 1361–1403, DOI: 10.1021/ja02242a004.

65 L. Qin, Y. Pan, F. Xie, L. Yu, R. Huai, L. Yang, D. Zhang and Z. Zhou, Rapid and selective adsorption capacity towards cationic dye with an anionic functionalized Anderson-type polyoxometalate, *Inorg. Chem. Commun.*, 2021, **133**, 108988, DOI: 10.1016/j.inoche.2021.108988.

66 J. Lan, Y. Wang, B. Huang, Z. Xiao and P. Wu, Application of polyoxometalates in photocatalytic degradation of organic pollutants, *Nanoscale Adv.*, 2021, **3**, 4646–4658, DOI: 10.1039/D1NA00408E.

67 K. Güneş, Isotherm and kinetic modeling of the adsorption of methylene blue, a cationic dye, on pumice, *Int. J. Chem. Technol.*, 2023, **7**, 67–74, DOI: 10.32571/ijct.1279701.

68 I. K. Konstantinou and T. A. Albanis, TiO2-assisted photocatalytic degradation of azo dyes in aqueous solution: kinetic and mechanistic investigations, *Appl. Catal., B*, 2004, **49**, 1–14, DOI: 10.1016/j.apcatb.2003.11.010.

69 Z. Sun, F. Li, M. Zhao, L. Xu and S. Fang, A comparative study on photoelectrochemical performance of TiO2 photoanodes enhanced by different polyoxometalates, *Electrochem. Commun.*, 2013, **30**, 38–41, DOI: 10.1016/j.elecom.2013.02.006.

70 J. Yu, T. Wang and S. Rtimi, Magnetically separable TiO2/FeOx/POM accelerating the photocatalytic removal of the emerging endocrine disruptor: 2,4-dichlorophenol, *Appl. Catal., B*, 2019, **254**, 66–75, DOI: 10.1016/j.apcatb.2019.04.088.

71 C. Díaz-Uribe, J. Viloria, L. Cervantes, W. Vallejo, K. Navarro, E. Romero and C. Quiñones, Photocatalytic Activity of Ag-TiO_2 Composites Deposited by Photoreduction under UV Irradiation, *Int. J. Photoenergy*, 2018, **2018**, 1–8, DOI: 10.1155/2018/6080432.

72 M. G. Kim, J. E. Lee, K. S. Kim, J. M. Kang, J. H. Lee, K. H. Kim, M. Cho and S. G. Lee, Photocatalytic degradation of methylene blue under UV and visible light by brookite–rutile bi-crystalline phase of TiO_2, New J, *Chem*, 2021, **45**, 3485–3497, DOI: 10.1039/D0NJ05162D.

73 W. Vallejo, G. Corzo, R. Berrio, C. Diaz-Uribe, F. Duran, X. Zarate and E. Schott, Synthesis and Characterization of TiO_2 Thin Films Modified with Anderson-Type Polyoxometalates (Ni, Co, and Fe), *Coatings*, 2024, **14**, 1362, DOI: 10.3390/coatings14111362.

74 M. Davis, F. Hung-Low, W. M. Hikal and L. J. Hope-Weeks, Enhanced photocatalytic performance of Fe-doped SnO_2 nanoarchitectures under UV irradiation: synthesis and activity, *J. Mater. Sci.*, 2013, **48**, 6404–6409, DOI: 10.1007/s10853-013-7440-4.

75 Q. Tang, X. An, H. Lan, H. Liu and J. Qu, Polyoxometalates/TiO2 photocatalysts with engineered facets for enhanced degradation of bisphenol A through persulfate activation, *Appl. Catal., B*, 2020, **268**, 118394, DOI: 10.1016/j.apcatb.2019.118394.

